RSC Advances

ROYAL SOCIETY OF CHEMISTRY

PAPER

View Article Online
View Journal | View Issue

Check for updates

Cite this: *RSC Adv.*, 2025, **15**, 26950

Effect of Ni on the performance of Ni–Zn-NC catalysts for CO hydrogenation to DME

Chunqiu Zhao,[ab] Qiang Chang,*[b] Fu Yin,[d] Jing Li,[e] Guowei Niu,[b] Hulin Wang,[b] Dan Liu,[c] Bhekie B. Mamba,[a] Chenghua Zhang*[bd] and Alex T. Kuvarega*[a]

Received 3rd July 2025
Accepted 17th July 2025

DOI: 10.1039/d5ra04740d

rsc.li/rsc-advances

One-step CO hydrogenation to value-added chemicals represents a prominent yet challenging research objective for conventional catalysis processes in chemical industry. Herein, we report a rationally designed Ni-doped Zn-NC catalyst embedded within an N-doped carbon matrix for one-step CO hydrogenation to dimethyl ether (DME), demonstrating superior CO conversion compared to the pristine Zn-NC catalyst (25.9% *vs.* 20.6%) while both maintaining high DME selectivity (>93%). Structural characterization revealed that Ni atoms existed in a bimetallic coordination environment, which is crucial for the promoting effect of Ni. In contrast, Ni nanoparticles incorporated into Zn-NC (nanoNi–Zn-NC) reduced CO conversion to less than 17% despite retaining high DME selectivity (>92%). Besides, control catalysts containing either Ni-only or Ni/Zn nanoparticles supported on carbon support exhibited limited catalytic activity and mainly produced hydrocarbons. This work provides valuable insights into the active sites of the bimetallic Ni–Zn-NC catalysts and elucidate the structural effects of bimetallic systems for CO conversion to DME. Furthermore, this study offers a feasible framework for optimizing Zn-based bimetallic catalysts.

1. Introduction

Converting the fossil fuels (coal, natural gas), through syngas chemistry, into value-added chemicals offers a promising alternative to its direct utilization and accordingly mitigates the adverse effects of fossil energy, *e.g.* greenhouse, pollution *etc.*[1,2] Among these chemicals, dimethyl ether (DME) stands out as an excellent substitute for fossil energy, mainly gasoline, due to its smokeless and absence of sulfur emissions.[3] To date, traditional multicomponent catalysts, such as CuZnAl combined with zeolite, have achieved CO hydrogenation to DME with conversion rates exceeding 50%.[4–6] Despite the ever-increasing research on one-step DME synthesis, it is still plagued by the complex catalyst components and the unwanted side reactions.[7] The structure–activity relationship remains ambiguous, primarily due to the intricate cross-phase interactions involving multiple metals in the catalysts.

To break through these limitations, single metal site catalysts with well-defined active sites,[8,9] especially single-atom catalysts that maximize atomic utilization, have demonstrated significant catalytic activity in various catalysis field, thereby attracting growing research interest in recent years. For instance, the Co–N–C catalyst with single-atom dispersion presents excellent chemoselectivity in nitroarenes hydrogenation.[10] The Zn-NC single atoms catalyst exhibits significant DME selectivity in CO hydrogenation.[11] However, the CO conversion performance has been constrained by the inherent limitation of having only a single metal–N active site. Therefore, developing highly dispersed bimetallic catalysts has emerges as a potential strategy to modulate CO activation capability through interatomic synergistic effects. This approach not only increases the number of active sites but also boost the catalytic activity of original active sites for the CO hydrogenation. Currently, a series of diatomic catalysts have explored across various catalytic applications.[12] Examples include Ni–Cu,[13] Ni–Fe,[14] Co–Zn,[15] Cu–Zn systems[16,17] which have demonstrated superior performance compared to their single metal atomic counterparts. Although these advances in bimetallic catalyst design for catalysis, critical challenges persist regarding the precise synthesis of well-defined bimetallic atomic structures, and the accurate identification of active site configurations. Moreover, achieving high metal loading while preventing the aggregation of bimetallic atoms during CO hydrogenation is crucial for

---

[a] Institute for Nanotechnology and Water Sustainability (iNanoWS), College of Science Engineering and Technology (CSET), University of South Africa, Florida Science Campus, Johannesburg, 1710, South Africa. E-mail: kuvarat@unisa.ac.za

[b] National Energy Center for Coal to Liquids, Synfuels China Co., Ltd, Huairou District, Beijing, 101400, China. E-mail: zhangchh@sxicc.ac.cn

[c] Tianjin Key Laboratory of Green Chemical Technology and Processes Engineering, School of Chemistry and Chemical Engineering, Tiangong University, Tianjin, 300387, China

[d] School of Chemistry and Chemical Engineering, Anhui University, Hefei, Anhui 230601, China

[e] State Key Laboratory of Coal Conversion, Institute of Coal Chemistry, Chinese Academy of Sciences, Taiyuan 030001, China

optimizing catalytic performance. Addressing these issues is essential for advancing the field and unlocking the full potential of bimetallic catalysts in the process of CO hydrogenation.

In this work, a highly dispersed bimetallic Ni–Zn catalyst supported on nitrogen-doped carbon was developed to enhance the catalytic performance of CO hydrogenation. Benefiting from the synergistic effect of highly dispersed Ni incorporated into the Zn-NC catalyst, the CO conversion was up to 25.9%, while maintaining a high DME selectivity of 93.9%. Raman spectroscopy analysis revealed that the heterocyclic carbon structure serves as a foundation for exposure of active sites, thereby improving CO hydrogenation. Comparative studies of these catalysts confirmed that the high concentration of Zn–Nx sites act as the primary effective active center, while the introduction of highly dispersed Ni positively promotes interactions with Zn in the Ni–Zn-NC catalyst, further enhancing its catalytic efficiency.

2. Experimental

2.1 Chemical reagents

2-methylimidazole (98%) was purchased from Aladdin. $Ni(NO_3)_2\cdot 6H_2O$ (98%) and $Zn(NO_3)_2\cdot 6H_2O$ (98.5%) were provided by Sinopharm Chemical Reagent Co., Ltd, China. *N*,*N*-dimethylformamide (99.8%) and methanol (99.8%) were supplied by Innochem Co., Ltd, China. HCl was purchased from Beijing Tongguang Fine Chemical Co., Ltd. Carbon nanotubes were produced by Synfuels China Technology Co., Ltd.

2.2 Preparation of catalysts

Typically, 0.44 g of $Ni(NO_3)_2\cdot 6H_2O$, 4.5 g of $Zn(NO_3)_2\cdot 6H_2O$ and 2-methylimidazole were dissolved in 150 ml of *N*,*N*-dimethylformamide and stirred at room temperature for 16 hours to obtain a homogeneous solution. The resulting solution was then transferred to a Teflon-lined autoclave and heated to 140 °C for 20 h. The bimetallic precursor was subsequently washed sequentially with DMF and methanol, followed by drying overnight at 65 °C to yield a solid precursor, denoted as Ni-doped ZIF. This solid precursor was calcined at 650 °C for 5 h under a nitrogen environment to obtain the target catalyst, labeled as Ni–Zn-NC. To prepare nanoNi–Zn-NC, the amount of $Ni(NO_3)_2\cdot 6H_2O$ was doubled compared to the original amount, while maintaining the same quantities of $Zn(NO_3)_2\cdot 6H_2O$ and 2-methylimidazole. The mixture was dissolved in *N*,*N*-dimethylformamide and stirred at room temperature for 16 hours to achieve a completely dissolved solution. The solution was then transferred to a Teflon-lined autoclave and treated at 140 °C for 30 h. The subsequent washing, drying, and calcination steps were identical to those used for Ni–Zn-NC. The Zn-NC catalyst was prepared using the same method, except that Ni source was not added. Ni-NC was synthesized by thermally calcining Ni-doped ZIF at 1000 °C for 10 h under a nitrogen atmosphere to evaporate the Zn species. To obtain Ni–Zn-NC-H, the Ni–Zn-NC catalyst was soaked in a HCl solution to remove most of Zn metal. Additionally, the Ni/Zn-CNT catalyst was prepared by impregnating 5 g carbon nanotubes with solution containing 9 g $Zn(NO_3)_2\cdot 6H_2O$ and 0.1 g $Ni(NO_3)_2\cdot 6H_2O$. After 24 h impregnation, the material was dried at 120 °C for 20 h and calcined at 650 °C under N_2 to obtain the final catalyst.

2.3 Characterization of catalysts

XRD patterns were acquired using a D8 Advance Bruker diffractometer equipped with Co Kα radiation operating at 40 mA and 35 kV. The samples were scanned over a 2θ range of 10 to 90° with a step of 0.02° and a residence time of 0.2 second per step.

BET specific surface area, pore size and pore volume size measurements were performed using ASAP 2420 equipment. Prior to analysis, each sample was degassed under vacuum at 90 °C for 8 h to remove the adsorbed impurities.

ICP-OES analysis was conducted on PerkinElmer Optima-2100DV to determine the metal content of catalysts. The sample were first calcined at 750 °C for 2 h and then immersed in aqua regia to dissolve the metal. Finally, the resulting solutions were analyzed using ICP-OES to quantify the metal content.

The contents of C and N elements were determined using an Organic Elemental Analyzer (Vario EL CUBE, Elementar, Germany). The analytical procedure involves combustion of the sample at high temperatures in an oxygen-rich environment, which converts carbon and nitrogen into their respective oxides (CO_2 and NO_x). Subsequently, helium is employed as the carrier gas to remove residual oxygen and transport the combustion products. The detector then quantitatively measures the concentrations of these elements through detection mechanisms.

Raman spectroscopy was carried out on a HORIBA LabRAM HR spectrometer equipped with 532 nm laser as the excitation source.

XPS spectra were collected using a Thermo ESCALAB 250Xi system with an Al Kα X-ray source. The energy resolution was maintained below 0.45 eV, and the sensitivity reached up to 100 k counts per second (cps) at a full width at half maximum (FWHM) of 0.5 eV.

TEM images were obtained using a Talos 200X microscope operated at an accelerating voltage of 200 kV. The samples were dispersed in ethanol, ultrasonicated for 10 min, and then dropped onto a copper grid coated with a holey carbon film for analysis.

2.4 Catalytic tests

The catalytic performance was evaluated using a fixed bed reactor. The catalyst was placed in the isothermal area of the reactor, while the remaining volume of the tube was filled with filler. The CO hydrogenation reactions were performed under the following conditions: a temperature of 350 °C (room temperature to 120 °C using 1 °C min^{-1}, and then to 350 °C at 0.5 °C min^{-1}), a gas hourly space velocity (GHSV) of 2000 h^{-1}, a pressure of 3 MPa, and a ratio H_2/CO of 1. The gaseous products were monitored in real-time using an online gas chromatography, while the non-gaseous products were analyzed offline. The catalytic activity was evaluated based on the CO conversion (X_{co}) and the selectivity of hydrocarbons (Cn) and dimethyl ether (DME), which were calculated using the following equations.

$$X_{co} = \frac{X_{coin} - X_{coout}}{X_{coin}} \times 100\% \quad (1)$$

$$S_{Cn} = \frac{S_{Cn}}{S\sum C} \times 100\% \quad (2)$$

$$S_{DME} = \frac{S_{DME}}{S\sum C} \times 100\% \quad (3)$$

In these equations: eqn (1): X_{co} represents the ratio of converted CO to the total number of CO in the feed gas. Eqn (2): S_{Cn} represents the selectivity of hydrocarbons (CH_4, C_{2+}), where the weight of the produced hydrocarbon is expressed as a percentage of the total hydrocarbons. Eqn (3): S_{DME} defines the selectivity of DME (CH_3OCH_3), where the weight of DME is expressed as a percentage of the total hydrocarbons.

3. Results and discussion

3.1 Structural characterizations of Ni–Zn catalysts

Given that the cavity diameter of ZIF-8 exceeds the size of a Ni atom, Ni has the potential to be encapsulated within the ZIF-8 skeleton.[14,18] As illustrated in Fig. 1a, the synthesized Ni-doped ZIF precursor retained the same structural characteristics as the pristine ZIF-8, confirming the successful incorporation of Ni atoms into the ZIF-8 structure. After pyrolysis at 650 °C, a highly dispersed bimetallic Ni–Zn catalysts supported on a nitrogen-doped carbon matrix was obtained. To investigate the synergistic effects between Ni and the Zn–Nx active sites in the Ni–Zn-NC catalyst, a series of comparative catalysts with different states of Ni and Zn were synthesized, including nanoNi–Zn-NC, Ni–Zn-NC–H, Ni/Zn-CNT, Ni-NC, and Zn-NC. These catalysts were employed to explore the influence of compositional and structural variations on catalytic performance.

The X-ray diffraction (XRD) patterns of Ni–Zn-NC, Ni–Zn-NC–H and Zn-NC catalysts exhibit no discernible metal diffraction peaks (Fig. 1b), which indicates high dispersion of metal species within the carbon matrix or ultrasmall metal particles. In addition, the XRD patterns of Ni–Zn-NC exhibit no diffraction peaks corresponding to metallic Ni or Zn crystals, in contrast to the Zn-NC reference. This confirms that appropriate Ni introduction did not compromise metal dispersion, with both elements existing predominantly in sub-5 nm clusters or atomic-scale. In contrast, the Ni-NC catalyst exhibits two well-defined diffraction peaks at 52.2 and 60.9° under Co Kα XRD irradiation, which are assigned to the (1 1 1) and (2 0 0) crystallographic planes of metallic Ni (PDF# 04-0850), respectively. In addition, compared with XRD pattern of Ni–Zn-NC, the diffraction peak of Ni metal in the nanoNi–Zn-NC catalyst exhibits a significant peak with increasing Ni content. Notably, no additional characteristic peaks corresponding to ZnO or NiO phases were observed. This phenomenon can be attributed to the high dispersion of Ni at low Ni contents, whereas at higher Ni contents, the Ni atoms tend to accumulate on the nitrogen-doped carbon matrix. Although no Zn compound was observed, the existence of diffraction peaks of Ni metal suggested that the crystal structure was affected by Ni amounts. Furthermore, the Ni/Zn-CNT catalyst exhibited uniformly dispersed Ni and the presence of a ZnO phase, these results reveal that pristine CNTs provide inferior metal dispersion compared to nitrogen-doped carbon supports. XRD analysis shows distinct diffraction peak of ZnO in CNT-supported catalyst, while Ni-doped ZIF derived counterparts exhibit no detectable crystallites, highlighting the distinct structural and compositional differences among the catalysts.

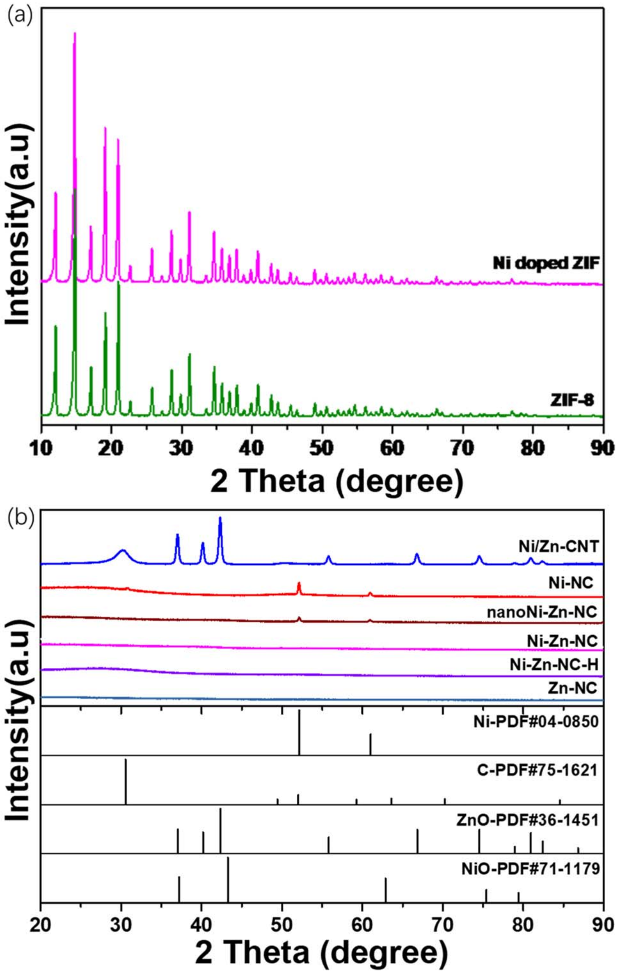

Fig. 1 XRD pattern of (a) Ni-doped ZIF and ZIF-8; (b) Zn-NC, Ni–Zn-NC, nanoNi–Zn-NC, Ni–Zn-NC–H, Ni/Zn-CNT, and Ni-NC catalysts.

The elemental composition, BET specific surface area, and pore structure parameters of the catalysts are displayed in Table 1. The Ni–Zn-NC catalyst contained 0.36 wt% Ni and 30.8 wt% Zn, with the Zn content being comparable to that of Zn-NC catalyst (29.2 wt%). Acid treatment of the Ni–Zn-NC (resulting in Ni–Zn-NC–H) significantly reduced the Zn content. In addition, the Ni content in Ni/Zn-CNT also remained at 0.34 wt%, while it increased to 1.20 wt% in both Ni-NC and nanoNi–Zn-NC catalysts. Fig. 2 presents the N_2 adsorption–desorption

Table 1 The ICP element content data and BET analysis data of Zn-NC, Ni–Zn-NC, nanoNi–Zn-NC, Ni–Zn-NC–H, Ni/Zn-CNT, and Ni-NC catalysts

Entry	Sample	Zn/wt%	Ni/wt%	C%m m^{-1}	N%m m^{-1}	V_{pore} (cm^3 g^{-1})	D_{pore} (nm)	BET/m^2 g^{-1}
1	Zn-NC	29.20	—	41.5	24.3	0.05	3.9	625
2	Ni–Zn-NC	30.80	0.36	39.1	22.4	0.02	3.3	533
3	nanoNi–Zn-NC	26.10	1.20	38.0	23.3	0.02	4.25	438
4	Ni–Zn-NC–H	3.70	0.34	50.8	29.6	0.07	3.50	966
5	Ni/Zn-CNT	28.85	0.34	68.1	0.1	0.35	12.18	100
6	Ni-NC	—	1.20	78.2	6.7	0.02	38.50	806

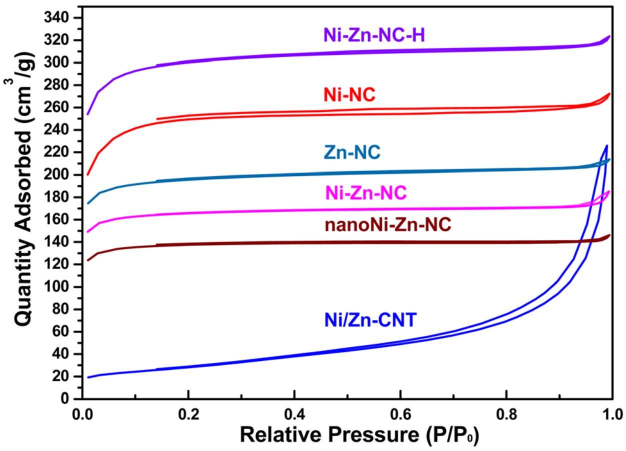

Fig. 2 N_2 sorption isotherms for all catalysts at 77 K.

isotherms of the samples. The isotherm of Ni/Zn-CNT, as classified by IUPAC standards, shows the hysteresis loop that contrasts with those observed in other containing N-doped carbon support catalysts. This difference in hysteresis behavior indicates substantial structural variations between ZIF-derived the N-doped carbon support and carbon nanotube supports. Specially, the specific surface area of Ni–Zn-NC can be kept at 533 m^2 g^{-1}. However, increasing the Ni loading, led to decreased specific surface area of the nanoNi–Zn-NC catalyst, while maintaining similar pore volume but larger pore size, suggesting partial pore occupation by Ni species. Consequently, the exposure of active sites may be influenced by these structural parameters, thereby potentially affecting the catalytic performance.

3.2 Evaluation of catalytic performance

The catalytic performances of CO hydrogenation over different Ni–Zn catalysts were performed on a fixed-bed reaction, and results are shown in Fig. 3. For the single metal catalysts, only Zn-NC demonstrated catalytic activity, achieving a CO conversion of 20.6% and DME selectivity of 95.6%, indicating that Zn species serve as the catalytic active sites for CO conversion, while Ni solely does not contribute to the DME formation. Compared with Zn-NC catalyst, the CO conversion of Ni–Zn-NC increased to 25.9% from 20.6% while maintaining the DME selectivity above 93%. Therefore, the introduction of a second metal in the catalyst mainly modulate the Zn coordination environment, thereby influencing the active sites and enhancing the reaction performance.[19,20] In contrast, when Ni existed as crystalline nanoparticles (as in the nanoNi–Zn-NC catalyst) not only does it fail to effectively modulate the Zn coordination environment, but also disrupted the intrinsic Zn–N active site structure. This detrimental effect caused the CO conversion to decline to 17.0%. Furthermore, this performance reduction can be attributed to Ni aggregation at higher loading levels, which can be confirmed by XRD and TEM results. These results unequivocally demonstrate that the dispersion state of the Ni species plays a pivotal role in determining the catalytic performance of Zn-NC catalyst. In addition, compared to the Ni–Zn-NC, the Ni–Zn-NC–H catalyst, with a Zn content of only 3.7 wt%, exhibited a CO conversion of just 1.5% and no DME selectivity, suggesting that the reaction could not proceed effectively when lacking sufficient Zn–N active sites. This underscores the critical role of Zn species in driving CO hydrogenation. Therefore, when the Zn state was changed to ZnO in the Ni/Zn-CNT catalyst, the CO conversion sharply decreased to 1.8%, with methane becoming the mainly product. The outcome was attributed to the absence of highly dispersed Zn, leading to a significant reduction in the Zn active sites. These findings highlight that the presence of appropriate Ni promotion and the highly dispersed abundant Zn in the Ni–Zn-NC catalyst is crucial for achieving enhanced catalytic performance.

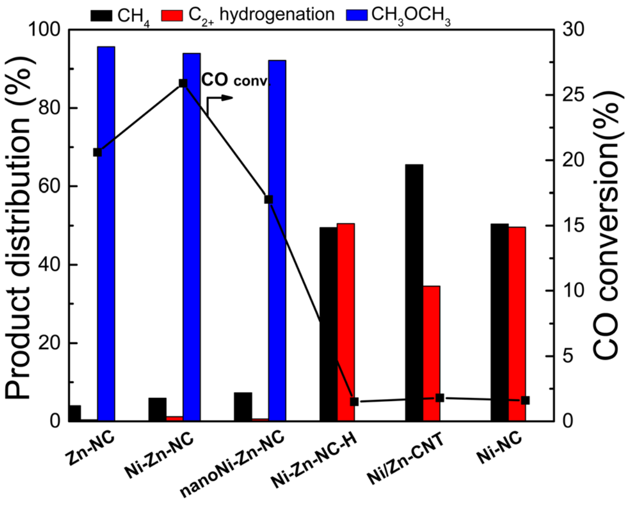

Fig. 3 The catalytic performance of CO hydrogenation to DME for all catalysts.

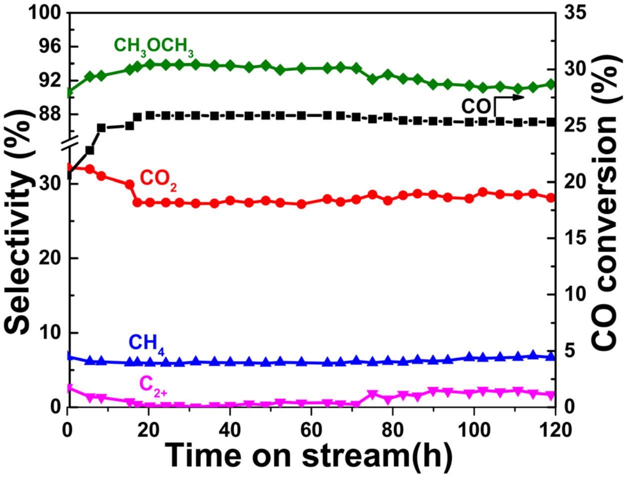

Fig. 4 Stability of the Ni–Zn-NC catalyst in the CO hydrogenation to DME reaction. (Reaction conditions: weight of the catalyst: 1.0 g, temperature: 350 °C, pressure: 3 MPa, gas: H_2/CO = 1).

Furthermore, the stability of the Ni–Zn-NC catalyst was investigated over 120 h (Fig. 4). The reaction reached steady-state conditions after 20 h, maintaining stable CO conversion at 26% and DME selectivity 93%. Only after 50 h, a slight decline for was observed, with CO conversion dropping from 26% to 25% and DME selectivity decreasing from 93% to 91%. This decline coincided with minor increase in C_{2+} hydrocarbon formation. Overall, these results demonstrate that the introduction of highly dispersed Ni effectively preserves the structural integrity and maintains good catalytic performance over extended period.

3.3 Microenvironmental information of catalysts

Using high-resolution transmission electron microscopy (TEM), the internal microstructure of samples, including crystal structure and morphology, can be observed. The TEM images of the catalysts are presented in Fig. 5. The Zn-NC catalyst exhibited a highly dispersed Zn, C, and N elements without detectable Zn lattice formation. The Ni and Zn elements in the Ni–Zn-NC catalyst were uniformly distributed within the N-doped carbon matrix, which was consistent with the XRD results. Furthermore, the high-magnification TEM image of Ni–Zn-NC obviously reveals the absence of metal lattice fringes in Ni–Zn-NC, with the carbon matrix exhibiting primarily amorphous carbon characteristics that facilitate the exposure and anchoring of M–Nx active sites, suggesting the presence of individual atoms metal species. In contrast, the mapping images of the nanoNi–Zn-NC catalyst show significant aggregation of Ni, accompanied by visible lattice fringes. The measured lattice spacing of 0.18 nm corresponds to the (200) plane of metallic Ni, whereas no lattice fringes associated with Zn were detected. These findings demonstrated two distinct states of Ni in the catalysts, with varying Ni content having no observable effect on the Zn species, thereby further corroborating the structural differences in Ni between Ni–Zn-NC and nanoNi–Zn-NC catalysts.

X-ray photoelectron spectroscopy (XPS) is an analytical technique that determines the elemental composition, chemical states, and molecular structure of the surface of a sample by measuring the photoelectrons emitted upon X-ray irradiation. In the N 1s XPS spectra (Fig. 6a), three peaks were observed at 398.8 eV, 399.7 eV, and 400.7 eV for all the catalysts except for Ni-NC, corresponding to the pyridinic-*N*, pyrrolic-*N*, and graphitic-*N*, respectively.[21] The peak at 399.7 eV could also be identified as metal–Nx,[22–24] indicating a strong interaction between nitrogen and metal atoms. The Ni-NC catalyst obtained through high-temperature pyrolysis exhibited a significant increase in graphitic nitrogen content. In contrast, the acid-washed Ni–Zn-NC–H sample showed decreased pyridinic nitrogen alongside increased pyrrolic nitrogen content,

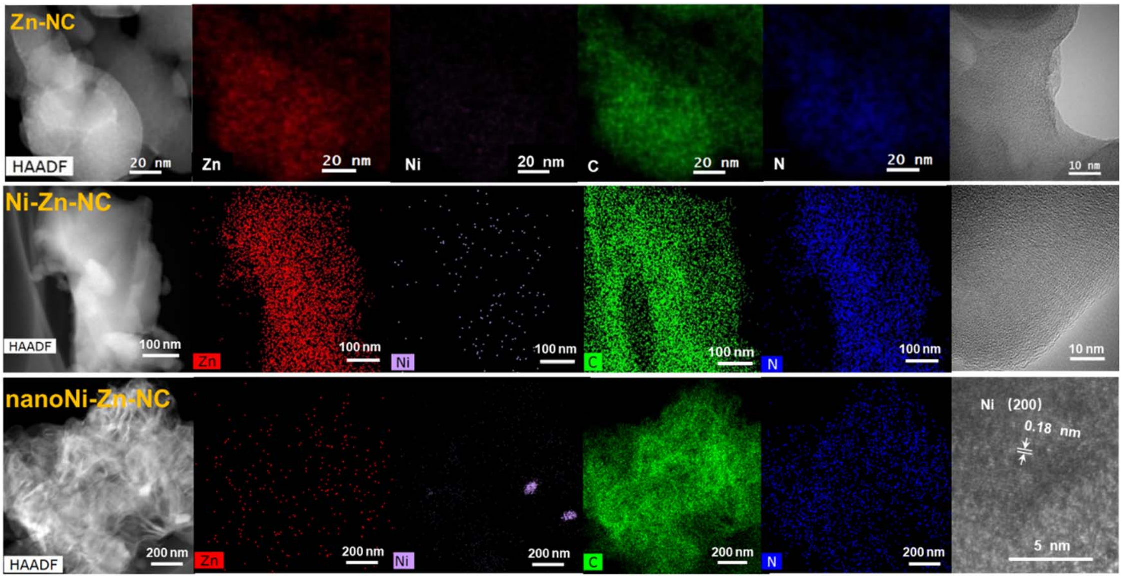

Fig. 5 TEM and EDS mapping of Zn-NC, Ni–Zn-NC, and nanoNi–Zn-NC catalysts.

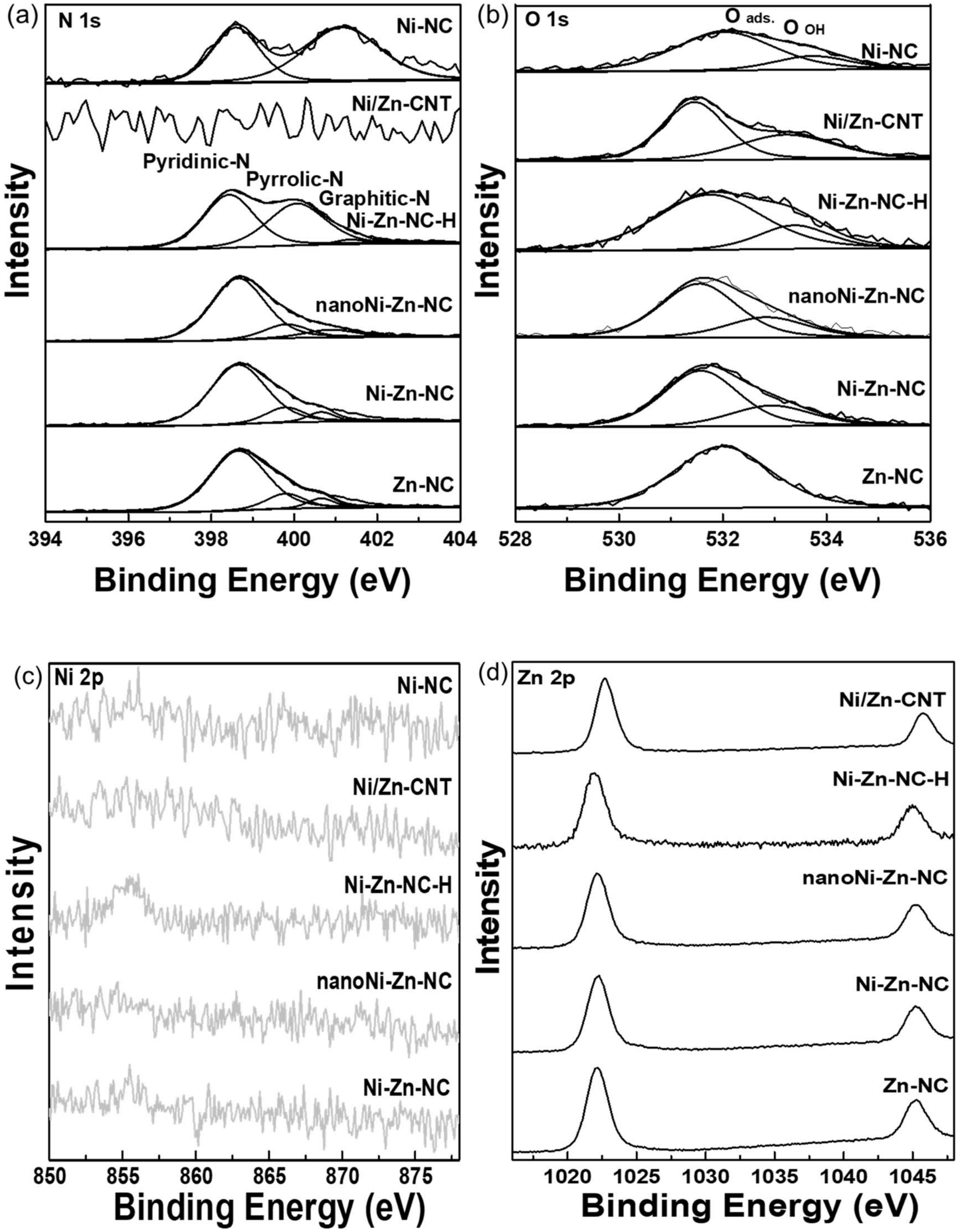

Fig. 6 XPS spectra of Zn-NC, Ni–Zn-NC, nanoNi–Zn-NC, Ni–Zn-NC–H, Ni/Zn-CNT, and Ni-NC catalysts (a) N 1s, (b) O 1s, (c) Ni 2p, (d) Zn 2p.

suggesting either the poor acid resistance of pyridinic nitrogen or nitrogen atom rearrangement (due to substantial metal removal) leading to pyrrolic nitrogen enrichment. In the O 1s spectra (Fig. 6b), the absence of metal–O bonds was observed in the all catalysts.[25] However, according to XRD results, the metal oxide was present in the Ni/Zn-CNT catalyst, suggesting that most ZnO was anchored within the nanotube pores. In contrast, the presence of oxide phases was ruled out for the other catalysts. In the Ni 2p spectra (Fig. 6c), the Ni 2p peak for Ni–Zn-NC was positioned between Ni^0 (853.5 eV) and Ni^{2+} (856.0 eV).[13,26] The Ni state in Ni–Zn-NC was also closer to that in nickel phthalocyanine (NiPc, which contains a Ni–N structure),[27] and it exhibited a higher binding energy compared to the nanoNi–Zn-NC catalyst. The Zn 2p XPS spectra (Fig. 6d) displayed two peaks associated with Zn^{2+}. Notably, the Zn state in Ni–Zn-NC was similar to that of Zn-NC, demonstrating that the introduction of

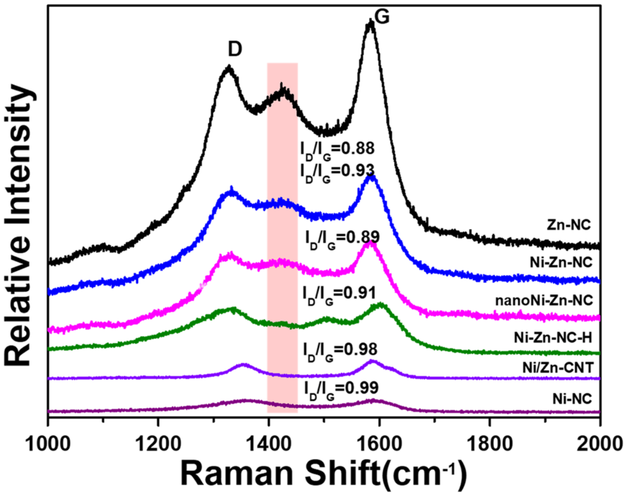

Fig. 7 Raman spectra of Zn-NC, Ni–Zn-NC, nanoNi–Zn-NC, Ni–Zn-NC–H, Ni/Zn-CNT, and Ni-NC catalysts.

Ni did not alter the Zn state. Based on these spectroscopic findings, both Ni and Zn were anchored within the amorphous carbon matrix through metal–Nx coordination structures, which may induce synergistic effects between the two metallic components. This configuration likely contributes to enhanced catalytic performances of the Ni–Zn-NC catalyst.

Raman spectra of all samples are shown in Fig. 7. The intensity of the D band peak at 1340 cm^{-1} and G band peak at 1583 cm^{-1} reflect the carbon defects and graphitization degree, respectively.[28,29] The intensity ratio of the D band to G band (I_D/I_G) reflects the level of carbon disorder, which indicates the relative number of defects sites. The Raman spectra of Ni–Zn-NC exhibit a higher I_D/I_G ratio compared to those of Zn-NC and nanoNi–Zn-NC catalysts, demonstrating a greater amount of amorphous carbon in Ni–Zn-NC. This amorphous carbon is advantageous as it provides more defect sites, which can serve as active sites for catalytic performance.[30,31] However, the Raman spectra of Zn-NC, Ni–Zn-NC and nanoNi–Zn-NC catalysts reveal a new peak at 1420 cm^{-1}, which is attributed to nitrogen-containing heterocyclic carbon structure.[32] The enhanced heterocyclic carbon peak is most likely attributed to C=N vibrations from pyridinic nitrogen. Among the various catalysts examined, the Zn-NC catalyst exhibited the most intense peak at 1420 cm^{-1}, which remained well-preserved in the Ni–Zn-NC catalyst but significantly diminished in the Ni–Zn-NC–H catalyst, consistent with the reduced pyridinic nitrogen content observed in XPS analysis. These findings demonstrate that the optimal anchoring sites for Ni–Zn species are associated with pyridinic nitrogen, thereby maintaining their highly dispersed state. Obviously, the introduction of highly dispersed Ni into the Zn-NC catalyst not only maintain this new peak at 1420 cm^{-1} but also increased the degree of

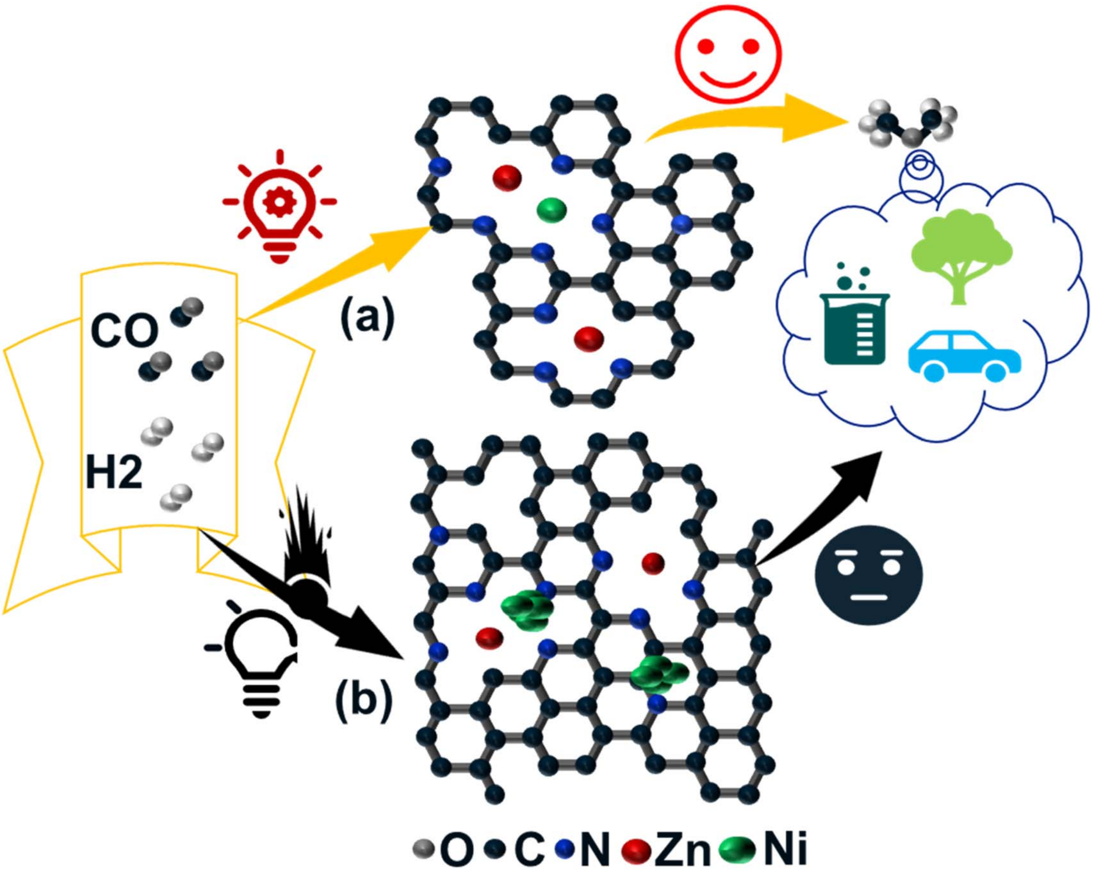

Fig. 8 The reaction scheme of the introduction for different state Ni, (a) Ni–Zn-NC and (b) nanoNi–Zn-NC catalyst.

carbon disorder. These structural modifications imply that the presence of Ni may alter the electronic or chemical properties of supports environment,[15] potentially contributing to the enhanced catalytic performance observed in Ni–Zn-NC catalyst.

3.4 Reaction mechanism of bimetallic Ni–Zn-NC catalyst

The catalytic formation of DME has been extensively investigated using Cu–Zn catalysts combined with alumina or molecular sieves, where the production efficiency is critically dependent on preparation methods, the proportional composition of two components and the precise control of the reaction conditions in bifunctional catalysts.[33] However, the necessity for the reaction to occur at two independent active sites, not only imposes limitations on the thermodynamic equilibrium but also predisposes the system to the generation of other hydrocarbons under sustained high-temperature reaction conditions.[34] Recent study has identified the Zn–N_3 site as an effective active center for catalyzing CO hydrogenation to DME.[11] While this site exhibits high selectivity for DME, there remains a substantial need to enhance its CO conversion efficiency. The introduction of a second metal component has been preliminarily established as a viable strategy to enhance the catalytic performance.[35] Building on these insights, a mechanistic pathway for CO conversion to DME over Ni–Zn-NC catalysts was proposed, as illustrated in Fig. 8. (Path a delineates the reaction route for the Ni–Zn-NC catalyst, whereas path b represents the reaction route for the nanoNi–Zn-NC catalyst). Comparative analysis reveals that the Ni–Zn-NC catalyst, featuring superior Ni dispersion on nitrogen-doped carbon support, facilitates a more effective coordination with Zn atoms compared to its nanoparticle counterpart. It also exhibits improved CO conversion activity and maintained DME production. These advancements underscore the potential of tailored catalyst design in optimizing catalytic processes for chemical synthesis.

4. Conclusion

In summary, Ni–Zn catalysts with tunable metals state and contents were performed under reaction conditions of 350 °C, H_2/CO ratio of 1, and 3 MPa. The optimal Ni–Zn-NC catalyst demonstrated superior performance with CO conversion of 25.9%, higher than that of both Zn-NC catalyst or Ni-NC catalyst. This enhancement stems from the ideal incorporation of Ni, maintaining high dispersion while preserving sufficient Zn content, which synergistically improves the interaction between Ni and Zn. This work systematically examines the impact of Ni state on catalytic performance and elucidated the role of Zn–N active site. The findings establish a strategic approach for optimizing the state of bimetallic Ni–Zn catalysts to enhance CO conversion efficiency.

Data availability

All data supporting the findings of this study are included within the manuscript.

Author contributions

C. Q. Z. executed the principal experiments and wrote the initial manuscript. Q. C. conducted comprehensive data analysis and participated in manuscript editing. F. Y., J. L., H. L. W. and G. W. N. performed material characterization through XPS, TEM tests and analysis. A. T. K., D. L. and B. B. M. provided the project supervision and manuscript revision. C. H. Z. conceived the research framework and supervised the project. All authors actively engaged in the work discussion and final approval of the submitted work.

Conflicts of interest

The authors declare no competing interests.

Acknowledgements

This work was supported by the National Key R&D Program of China (2022YFB4101200), the National Natural Science Foundation of China (22302219, 22179001) and Synfuels China Technology Co., Ltd.

References

1 A. A. Al-Qadri, G. A. Nasser, H. Adamu, O. Muraza and T. A. Saleh, *J. Energy Chem.*, 2023, **79**, 418–449.
2 U. Mondal and G. D. Yadav, *J. CO_2 Util.*, 2019, **32**, 299–320.
3 W. A. Pamungkas, A. W. Budiman, B. S. T. Inayati, D. Mersitarini, D. Ardyatna and I. Mahendra, *E3S Web of Conferences*, 2024, p. 481.
4 K. Saravanan, H. Ham, N. Tsubaki and J. W. Bae, *Appl. Catal., B*, 2017, **217**, 494–522.
5 M. Gentzen, W. Habicht, D. E. Doronkin, J. D. Grunwaldt, J. Sauer and S. Behrens, *Catal. Sci. Technol.*, 2016, **6**, 1054–1063.
6 J. Sun, G. Yang, Y. Yoneyama and N. Tsubaki, *ACS Catal.*, 2014, **4**, 3346–3356.
7 J Palomo, M. Á Rodríguez-Cano, J. Rodríguez-Mirasol and T. Cordero, *Appl. Catal., B*, 2020, **270**, 118893.
8 H. Jiang, H. Bongard, W. Schmidt and F. Schüth, *Microporous Mesoporous Mater.*, 2012, **164**, 3–8.
9 C. Liu, J. Kang, Z. Q. Huang, Y. H. Song, Y. S. Xiao, J. Song, J. X. He, C. R. Chang, H. Q. Ge, Y. Wang, Z. T. Liu and Z. W. Liu, *Nat. Commun.*, 2021, **12**, 2305.
10 W. Liu, L. Zhang, W. Yan, X. Liu, X. Yang, S. Miao, W. Wang, A. Wang and T. Zhang, *Chem. Sci.*, 2016, **7**, 5758–5764.
11 C. Zhao, J. Liu, Y. Wei, T. Shi, J. Xue, Q. Chang, S. Sun, D. Liu, A. T. Kuvarega, B. B. Mamba and C. Zhang, *ACS Appl. Nano Mater.*, 2024, **7**, 2224–2231.
12 S. Chen, M. Cui, Z. Yin, J. Xiong, L. Mi and Y. Li, *ChemSusChem*, 2020, **14**, 73–93.
13 H. Cheng, X. Wu, M. Feng, X. Li, G. Lei, Z. Fan, D. Pan, F. Cui and G. He, *ACS Catal.*, 2021, **11**, 12673–12681.
14 W. Ren, X. Tan, W. Yang, C. Jia, S. Xu, K. Wang, S. C. Smith and C. Zhao, *Angew. Chem., Int. Ed.*, 2019, **58**, 6972–6976.

15 W. Zhu, L. Zhang, S. Liu, A. Li, X. Yuan, C. Hu, G. Zhang, W. Deng, K. Zang, J. Luo, Y. Zhu, M. Gu, Z. J. Zhao and J. Gong, *Angew. Chem., Int. Ed.*, 2020, **59**, 12664–12668.

16 G. Dong, G. Wang, Y. Hu, M. Li, J. Cheng and D. Geng, *Appl. Surf. Sci.*, 2024, 660.

17 C. An, S. Wu, R. Huang, X. Chen, X. Han, H. Gomaa, Q. Deng, L. Zhao and N. Hu, *Chem. Eng. J.*, 2023, 471.

18 C. Zhao, X. Dai, T. Yao, W. Chen, X. Wang, J. Wang, J. Yang, S. Wei, Y. Wu and Y Li, *J. Am. Chem. Soc.*, 2017, **139**, 8078–8081.

19 S. Pu, L. Sun, C. Yang, J. Chu, Y. Wang, C. Min, X. Zou and C. Zhuang, *Mol. Catal.*, 2024, 559.

20 F. Ma and X. Chen, *ACS Appl. Nano Mater.*, 2023, **6**, 16546–16554.

21 Q. Yang, C. C. Yang, C. H. Lin and H. L. Jiang, *Angew. Chem., Int. Ed. Engl.*, 2019, **58**, 3511–3515.

22 Y. Guo, L. Feng, C. Wu, X. Wang and X. Zhang, *J. Catal.*, 2020, **390**, 213–223.

23 L. Zhang, G. Fan, W. Xu, M. Yu, L. Wang, Z. Yan and F. Cheng, *Chem. Commun.*, 2020, **56**, 11957–11960.

24 D. Liu, K. Srinivas, A. Chen, F. Ma, H. Yu, Z. Zhang, M. Wang, Y. Wu and Y. Chen, *J. Colloid Interface Sci.*, 2023, **635**, 578–587.

25 S. Wang, J. Yang, S. Wang, N. Zhao and F. Xiao, *Fuel Process. Technol.*, 2023, 247.

26 J. Li, Z. Cao, X. Zhang, L. Gao, X. Liu, L. Chen, Y. Zhang, Q. Zhang, P. Zhang and T. Liu, *Mol. Catal.*, 2024, 558.

27 T. Zhang, X. Han, H. Yang, A. Han, E. Hu, Y. Li, X. Q. Yang, L. Wang, J. Liu and B. Liu, *Angew. Chem., Int. Ed. Engl.*, 2020, **59**, 12055–12061.

28 J. Yan, X. Zheng, C. Wei, Z. Sun, K. Zeng, L. Shen, J. Sun, M. H. Rümmeli and R. Yang, *Carbon*, 2021, **171**, 320–328.

29 J. Yan, M. Tian, R. Shi, T. Gu, K. Zeng, J. Zhou, Q. Zhang, M. H. Rümmeli and R. Yang, *Mater. Today Energy*, 2022, 30.

30 Z. Wang, C. Li, Y. Liu, Y. Wu, S. Zhang and C. Deng, *J. Energy Chem.*, 2023, **83**, 264–274.

31 J. Pei, T. Wang, R. Sui, X. Zhang, D. Zhou, F. Qin, X. Zhao, Q. Liu, W. Yan, J. Dong, L. Zheng, A. Li, J. Mao, W. Zhu, W. Chen and Z. Zhuang, *Energy Environ. Sci.*, 2021, **14**, 3019–3028.

32 X. Bai, P. Hu, A. Li, Y. Zhang, A. Li, G. Zhang, Y. Xue, T. Jiang, Z. Wang, H. Cui, J. Kang, H. Zhao, L. Gu, W. Zhou, L.-M. Liu, X. Qiu and L. Guo, *Nature*, 2024, **634**, 80–84.

33 J. L. Weber, C. H. Mejía, K. P. de Jong and P. E. de Jongh, *Catal. Sci. Technol.*, 2024, **14**, 4799–4842.

34 M. Gentzen, D. E. Doronkin, T. L. Sheppard, J. -D. Grunwaldt, J. Sauer and S. Behrens, *Appl. Catal., A*, 2018, **557**, 99–107.

35 X. Yang, L. Xu and Y. Li, *Coord. Chem. Rev.*, 2024, **516**, 215961.